Korean J. Chem. Eng., 32(12), 2384-2393 (2015)
DOI: 10.1007/s11814-015-0033-y

pISSN: 0256-1115
eISSN: 1975-7220

Microscopic flow characteristics in fluidized bed of cylinder-shaped particles

Chunhua Wang*,†, Zhaoping Zhong, and Xiaoyi Wang****

*College of Energy & Power Engineering, Nanjing University of Aeronautics and Astronautics, Nanjing 210016, China
**Key Laboratory of Energy Thermal Conversion and Control of Ministry of Education,
School of Energy and Environment, Southeast University, Nanjing 210096, China
(*Received 23 October 2014 • accepted 9 February 2015*)

Abstract–IBM (Immersed boundary method) and DEM (Discrete element method) coupling method were used to simulate the flow of cylinder-shaped particles in a fluidized bed. The greatest advantage of IBM-DEM is that it can reveal the microscopic characteristics of dense-phase gas-particle flow in Cartesian grids. Large cylinder-shaped particles are very difficult to fluidize, and slugging flow can be observed even if the static bed height is low. The gas flow field around the particle in fluidized bed is analyzed, and the formation and development of vortex behind the particle is affected obviously by the neighboring particles. Particle trajectory is obtained, and the effect of gas phase on particle rotation becomes active as particle size increases. Compared with the experimental results, the gas-solid force in simulation results is higher. This calculation error may be reduced by decreasing the grid size.

Keywords: Fluidization, Immersed Boundary Method, Discrete Element Method, Simulation

INTRODUCTION

DEM (Discrete element method) and CFD (Computational fluid dynamics) coupling method were initially proposed by Tsuji et al. [1], and used to simulate a gas-solid flow in a fluidized bed. The most valuable advantage of the CFD-DEM method is that the trajectory of every particle can be traced. In CFD-DEM, the movement of the gas phase is controlled by the continuity equation and Navier-Stokes equations; the contacting force caused by particle collision or particle-wall collision is solved by the discrete element method [2]; and point-to-source model is applied to calculate the momentum coupling between gas and solid phases. The CFD-DEM method has been widely used for the simulation of dense gas-solid flow [3], such as bubbling fluidized bed[4], spouted bed [5,6], and rotating fluidized bed [7].

For the accuracy of a point-to-source model, the grid size for gas flow in the traditional CFD-DEM method should be much larger than the particle size; therefore, the traditional CFD-DEM belongs to mesoscopic simulation. In a mesoscopic grid, which is shown in Fig. 1(a), there are several particles in one grid, but the gas flow field is expressed by phase-volume averaged variables in the grid, hence the effect of subgrid structure of both phases is not including the momentum coupling. Especially for the cases of large particles and relatively small container, it is difficult to separate the subgrid scale and overgrid scale. So it is necessary to develop a microscopic simulation method. There are some researches on microscopic simulation of dense gas-solid flows, such as the research of Kuwagi et al. [8], Hoef et al. [9], Ma et al. [10], Wang et al. [11].

An immersed boundary method (IBM) was initially provided by Peskin [12] and used for the numerical analysis of blood flow in the heart. In the IBM, a body in the flow field is considered a kind of momentum forcing in N-S equations, and flow over a complex geometry can be easily simulated in Cartesian or cylindrical grid, which means that an unstructured grid is not necessary and can save much computation time. Because of these advantages, the IBM has become very attractive, and is often used to simulate flow field around a body with irregular shape, such as spherical particles [13, 14], heart valves [15], and immersed tube [16]. The IBM can handle the interaction between spherical particles and gas phase in Cartesian grids easily, which is shown in Fig. 1(b), and the DEM can solve the particle-particle collision and particle-wall collision. In this research, the IBM improved by Kajishima et al. [17] was coupled with the DEM to simulate the particle flow in fluidized bed.

In this study, the basic theories of IBM and DEM were introduced first, and then the flow of cylinder-shaped particles in fluidized bed was simulated, finally, the simulation results were analyzed combined with experimental result.

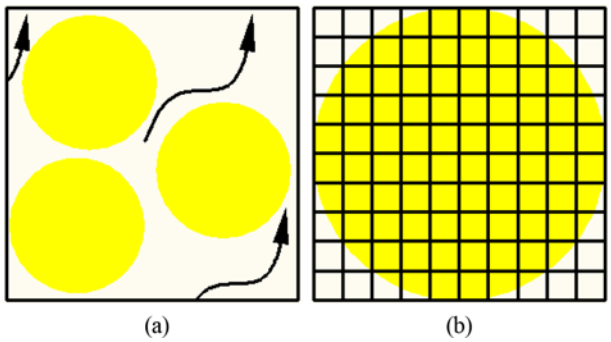

Fig. 1. Grids for mesoscopic and microscopic simulation. (a) For traditional DEM-CFD; (b) for immersed boundary method.

†To whom correspondence should be addressed.
E-mail: chunhuawang@nuaa.edu.cn

BASIC THEORIES FOR IBM-DEM

1. Immersed Boundary Method

Kajishima et al. define the solid volume-weighted velocity, **u**, as [17]:

$$\mathbf{u}=(1-\alpha)\mathbf{u}_f+\alpha\mathbf{u}_p \tag{1}$$

where, α is the solid volume fraction, $\mathbf{u}_f$ is the gas velocity, and $\mathbf{u}_p$ is the velocity inside the particle. According to IBM, the continuity and N-S equations for gas phase can be transformed to:

$$\nabla\cdot\mathbf{u}=0 \tag{2}$$

$$\frac{\partial\mathbf{u}}{\partial t}=-\frac{1}{\rho_f}\nabla P+\boldsymbol{\tau}+\mathbf{f} \tag{3}$$

$$\boldsymbol{\tau}=-\mathbf{u}\cdot\nabla\mathbf{u}+\nu_f\nabla\cdot[\nabla\mathbf{u}+(\nabla\mathbf{u})^T]+\mathbf{g} \tag{4}$$

where, P is the statistic pressure, ρ_f is the gas density, **g** is the gravity, ν_f is the gas kinematic viscosity. **f** is the gas-solid volume force, and can be expressed by:

$$\mathbf{f}=\alpha(\mathbf{u}_p-\hat{\mathbf{u}})/\Delta t \tag{5}$$

$$\hat{\mathbf{u}}=\mathbf{u}^n+\Delta t\left(-\frac{1}{\rho_f}\nabla P+\boldsymbol{\tau}\right) \tag{6}$$

The particle motion can be calculated by the following equations:

$$\frac{d(m_p\mathbf{v}_p)}{dt}=-\rho_f\int_{volume}\mathbf{f}dV+m_p\mathbf{g}+\mathbf{F}_c \tag{7}$$

$$\frac{d(I_p\cdot\omega_p)}{dt}=-\rho_f\int_{volume}\mathbf{r}\times\mathbf{f}dV+\mathbf{N} \tag{8}$$

where, I_p is the inertial tensor, m_p is the particle mass, $\mathbf{F}_c$ is the collision force, **r** is the relative position from the particle center to the computational cell, ω_p is the angular velocity, **N** is the collision torque. $\mathbf{v}_p$ is the particle translation velocity, and the relation between $\mathbf{v}_p$ and $\mathbf{u}_p$ can be expressed by:

$$\mathbf{u}_p=\mathbf{v}_p+\mathbf{r}\times\mathbf{w}_p \tag{9}$$

2. Discrete Element Method

In the DEM, which was initially proposed by Cundall and Strack [2], collision between particles is modeled by springs, dashpots and a slider, which is shown in Fig. 2. Contacting force in DEM is divided into normal force $\mathbf{f}_{cn}$ and tangential force $\mathbf{f}_{ct}$, and they can be calculated by Eqs. (10) and (11), respectively.

$$\mathbf{f}_{cn}=-k_n\mathbf{d}_n-\eta\mathbf{v}_n \tag{10}$$

$$\mathbf{f}_{ct}=-k_t\mathbf{d}_t-\eta\mathbf{v}_t \tag{11}$$

where, d_n and d_t represent the particle displacement in the normal direction and tangential direction, respectively, $\mathbf{v}_n$ and $\mathbf{v}_t$ is the particle relative velocity in the normal direction and tangential direction, respectively, k is the spring stiffness, and η is the coefficient of viscous dissipation. If $|\mathbf{f}_{ct}|>\mu_f|\mathbf{f}_{cn}|$ is satisfied, $\mathbf{f}_{ct}$ should be calculated by Eq. (12).

$$\mathbf{f}_{ct}=-\mu_f|\mathbf{f}_{cn}|\mathbf{t} \tag{12}$$

where, μ_f is the coefficient of friction.

The coefficient of viscous dissipation, η, can be calculated by the following equations [18]:

$$\eta=2\gamma(mk)^{0.5} \tag{13}$$

$$\gamma=\alpha/(1+\alpha^2)^{0.5} \tag{14}$$

$$\alpha=-(1/\pi)\ln e \tag{15}$$

where, e is the restitution coefficient of spring.

To determine the direction of contacting force, a cylinder-shaped particle is usually described by the agglomeration of many fictitious spheres, and the collision between the cylinder-shaped particles is transformed to that between the fictitious spheres [19,20]. Three agglomeration styles of fictitious spheres have been commonly used, and these styles are shown in Fig. 3. Because the diameter and length of the cylinder-shaped particle in this research are the same, the first two methods are not suitable, and the third method is used in this research. In the third method, the cylinder-shaped particle is described by the agglomeration of seven fictitious cylinder-shaped particles, and every fictitious cylinder-shaped particle is assumed to be the agglomeration of three fictitious spheres.

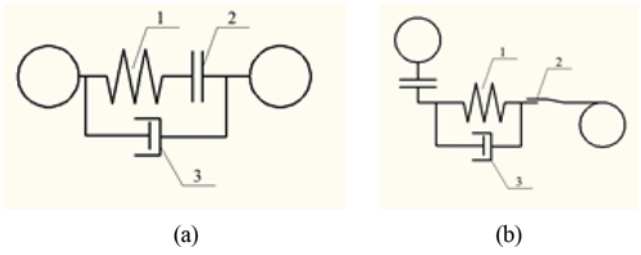

Fig. 2. Mathematical model for discrete element method. (a) Normal direction; (b) tangential direction.
1. Spring 2. Slider 3. Dashpot

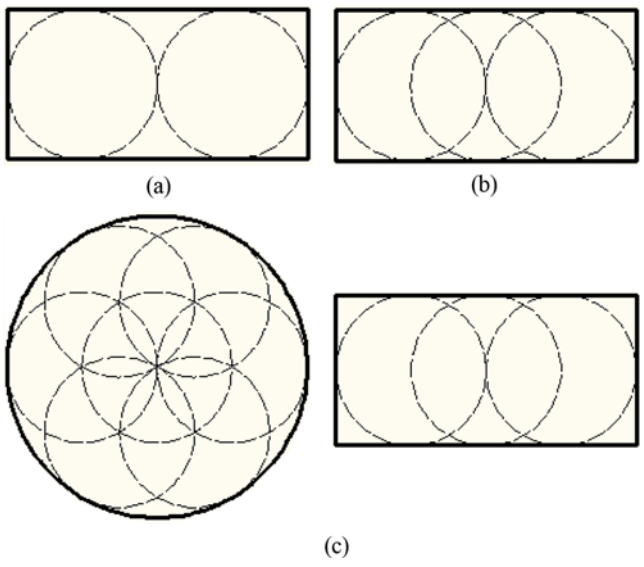

Fig. 3. Multi-element method for cylinder-shaped particle. (a) Two-sphere method; (b) three-sphere method; (c) multi-sphere method.

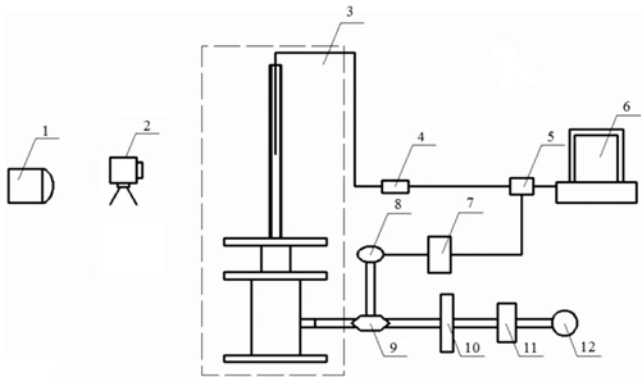

Fig. 4. Schematic of the experimental set-up.

1. Halogen lamp
2. High speed camera
3. Fluidized bed
4. Pressure transducer
5. A/D converter
6. Terminal computer
7. Dynamic strain amplifier
8. Strain pressure recorder
9. Laminar flow meter
10. Regulator
11. Thermometer
12. Compressor

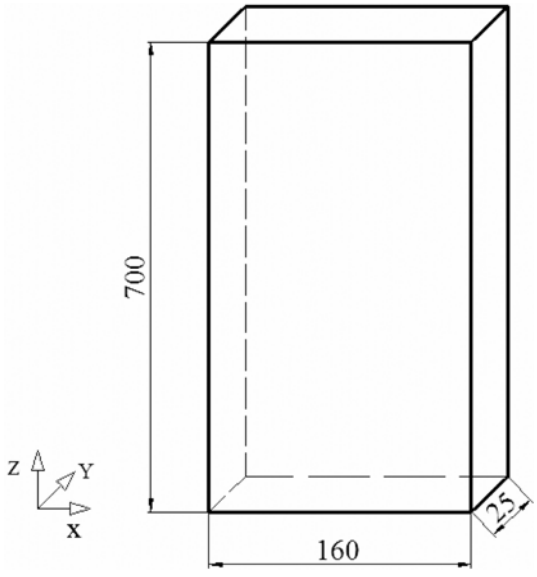

Fig. 5. Geometry of fluidized bed.

EXPERIMENTAL AND SIMULATION SYSTEM

1. Experimental System

A detailed schematic of the experimental set-up is shown in Fig. 4. The fluidized bed is made of Plexiglas, its geometry is shown in Fig. 5. To facilitate the analysis, the x direction is defined as the radial direction. The fluidization air is supplied by Roots blower (DSL-50, Guangyu Mechanical Co., China), and measured by mass flow meter (3095MV, Emerson Electric Co. USA). The maximum air flow supplied by the Roots blower is 90 Nm^3/h, and the measurement error of mass flow meter is less than ±1%. The flow of the solid phase is shot by high speed camera (Phantom V640, York Technology Co. Ltd., USA), which is used to compare with the simulation results. Pressure sampling system consisted of differential pressure sensor (ES-30, Essen Electronics Technology Co. Ltd., China), A/D converter (USB-6251, National Instruments Co., USA) and terminal computer (Thinkpad X240, Lenovo Group Co. Ltd., China) is used to determine the minimum fluidization velocity. Two pressure taps are located 10 mm below the air distribution plate and 200 mm above the air distribution plate, respectively. The sampling frequency is 600 Hz. The diameter and length of the cylinder-shaped particle is both 10 mm.

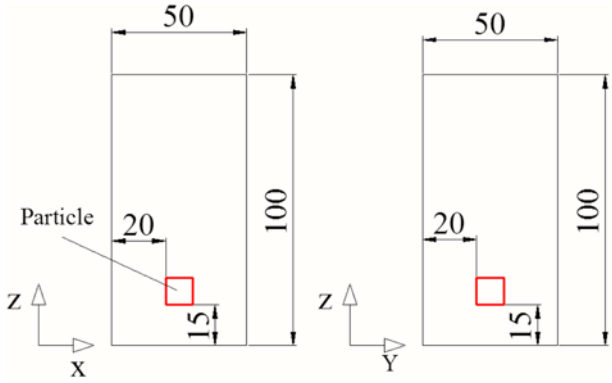

Fig. 6. Geometry of computational domain for grid size test.

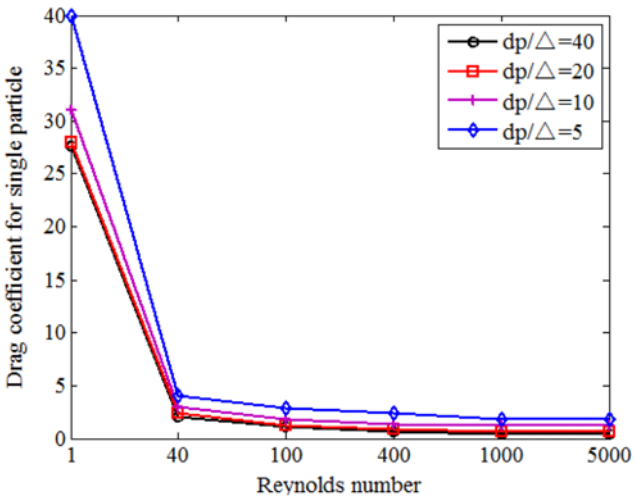

Fig. 7. Influence of grid size on drag coefficient for single particle.

2. Simulation System

The calculation accuracy of Kajishima's IBM depends to a large extent on the grid size. To determine the optimal grid size, the gas flow around the fixed cylinder-shaped particle in the vertical channel is simulated with different grid sizes. The geometry of computation domain is shown in Fig. 6. The drag coefficient C_D is defined as:

$$C_D = \frac{2F_d}{\rho_f u_{fs}^2 A} \tag{16}$$

where, F_d is the drag force component in the direction of the gas flow, ρ_f is the gas density, u_{fs} is the speed of the particle relative to the fluid, and A is the particle projected area. Fig. 7 shows the variation of C_D with grid size. C_D value decreases with the increase of d_p/Δ first, and then keeps constant as d_p/Δ reaches about 20 (d_p is the particle size, and Δ is the grid size). Based on the overall analysis of calculation accuracy and cost, d_p/Δ was selected as 15 in this

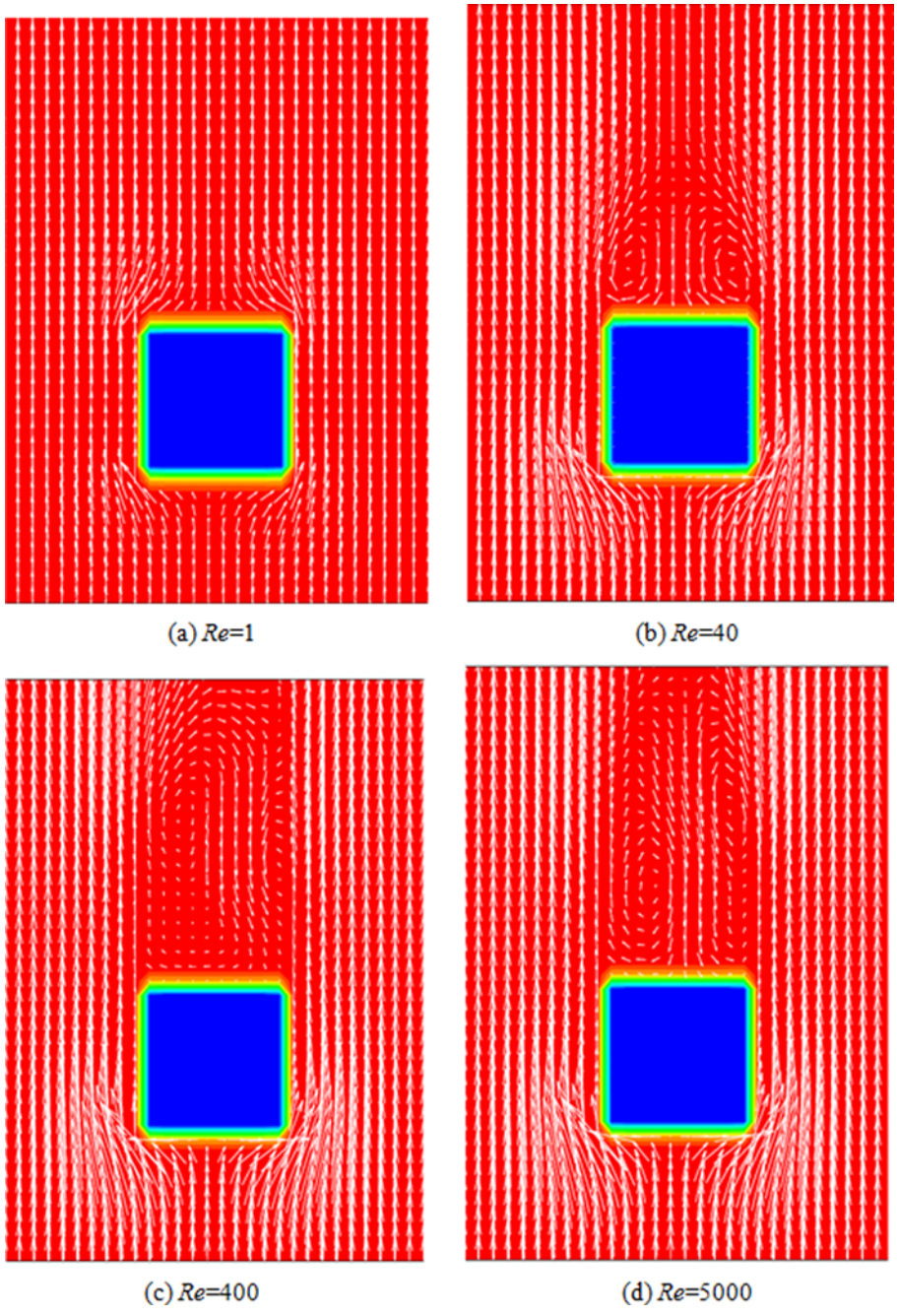

Fig. 8. Gas flow past a single cylinder-shaped particle in the simulation result.

paper. Fig. 8 shows the flow round the particle in the simulation results with $d_p/\Delta=15$. As the Reynolds number is very small, the shape of every streamline is symmetrical, not only around the cylinder's left and right side, but also around its upper and lower. As Reynolds number is between 1-60, the flow separates from the rear of the cylinder, and a symmetric pair of vortices is formed in the near wake. As Reynolds number exceeds 60, the rear flow becomes unstable, and the vortex begins to oscillate regularly. As Reynolds number reaches 1000, the vortices are mixed together, and the flow behind the cylinder behaves very irregularly and space scale.

In a staggered grid, FVM (Finite volume method) was applied for discretization of the differential equations, and SIMPLE (Semi-implicit method for pressure linked equations) algorithm was used to solve gas pressure and velocity. Non-slip, pressure outlet and velocity inlet boundary conditions were set to determine the boundary parameters near the wall, outlet and inlet respectively in this research. Under the velocity inlet condition, the velocity field is supplied, and, for consistency, the boundary condition on pressure is zero gradient. Under the pressure outlet condition, the pressure field is supplied, and the boundary condition on velocity is zero gradient. Under the non-slip boundary condition, the fluid velocity relative to the wall is zero, and the pressure is specified zero gradient since the flux through the wall is zero. Two-way coupling method was used to couple particle and gas motion. The simulation parame-

Table 1. Simulated system parameters in this research

Parameters	Unit	Value
Particle size	mm	10×10
Grid size	d_p/Δ	15
Particle density	kg/m^3	900
Time step	s	5×10^{-6}
Static bed height	mm	50,70
Restitution coefficient		0.59
Coefficient of particle-particle friction		0.64
Coefficient of particle-wall friction		0.34
Poisson ratio of particle (wall)		0.33 (0.33)
Elasticity modulus of particle (wall)	N/m^2	3×10^9 (3×10^9)
Spring stiffness on normal direction*	N/m	810
Spring stiffness on tangential direction*	N/m	260

*The spring stiffness was calculated by Hertz-Mindlin method [21]

ters for fluidized bed are listed in Table 1. The particle material in current research is the same as that in Ref. [20], so, DEM parameters of the particles in Table 1 are obtained from Ref. [20].

SIMULATION RESULTS

1. Comparison between the Simulation and Experimental Results

Figs. 9 and 10 show snapshots of the particle flow in the simulation results and experimental results (H_0 is static bed height, and u_s is the gas velocity). In the upper region of the bed, all the particles move upward like a plug, and a large bubble can be observed. The formation of the large bubble can be attributed to the horizontal diffusion of jet gas. This flow pattern is a typical 'slugging' flow. Usually, 'slugging' flow takes place when the static bed height is high [22]. However, in the current research, the large particles are very difficult to fluidize, and 'slugging' flow can be observed even if the static bed height is not high. Fig. 11 shows the power spectrum density analysis of pressure signals in simulation and experimental results, and the dominant frequency can be observed clearly. In 'slugging' flow, a large bubble forms, grows and bursts frequently, and the pressure fluctuation signals show periodical characteristic

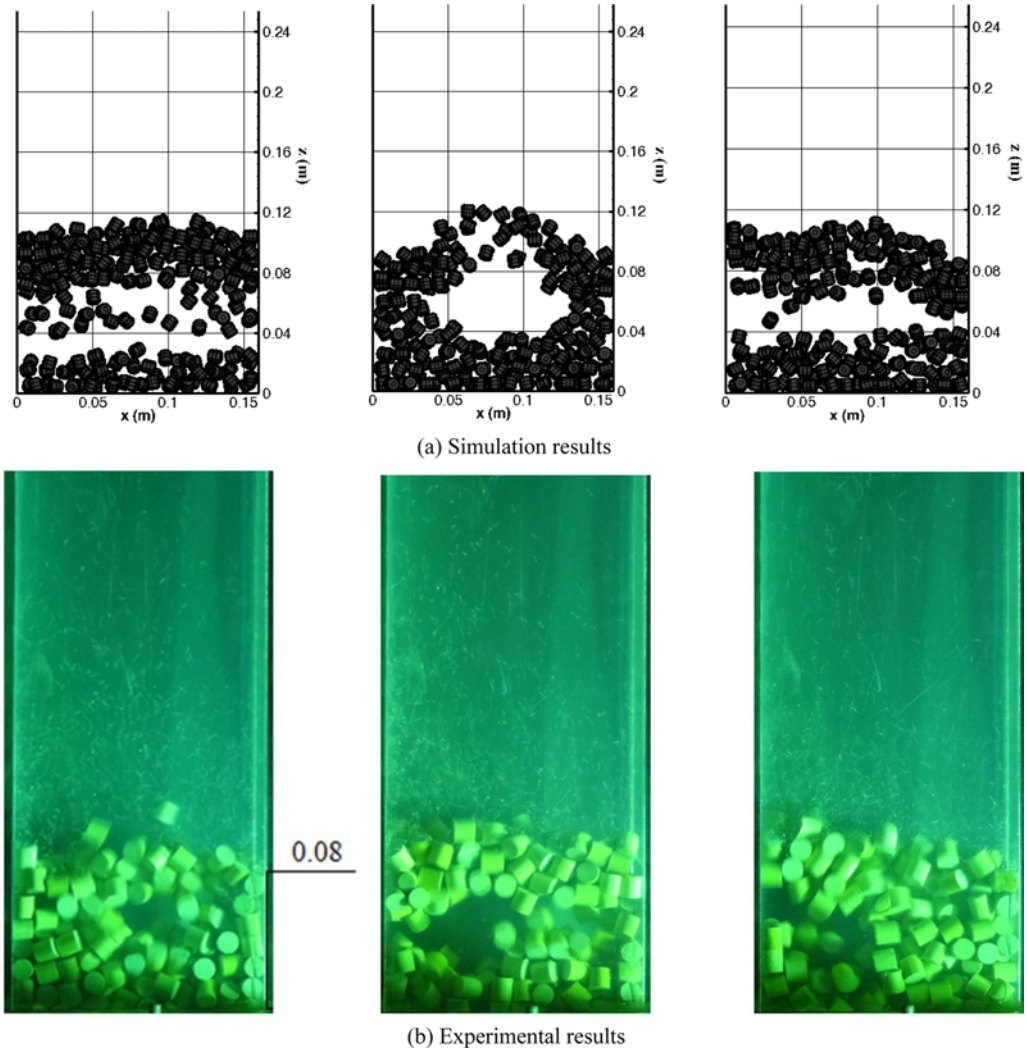

Fig. 9. Comparison of flow patterns in simulation results and experimental results (H_0=50 mm, u_s=2.8 m/s).

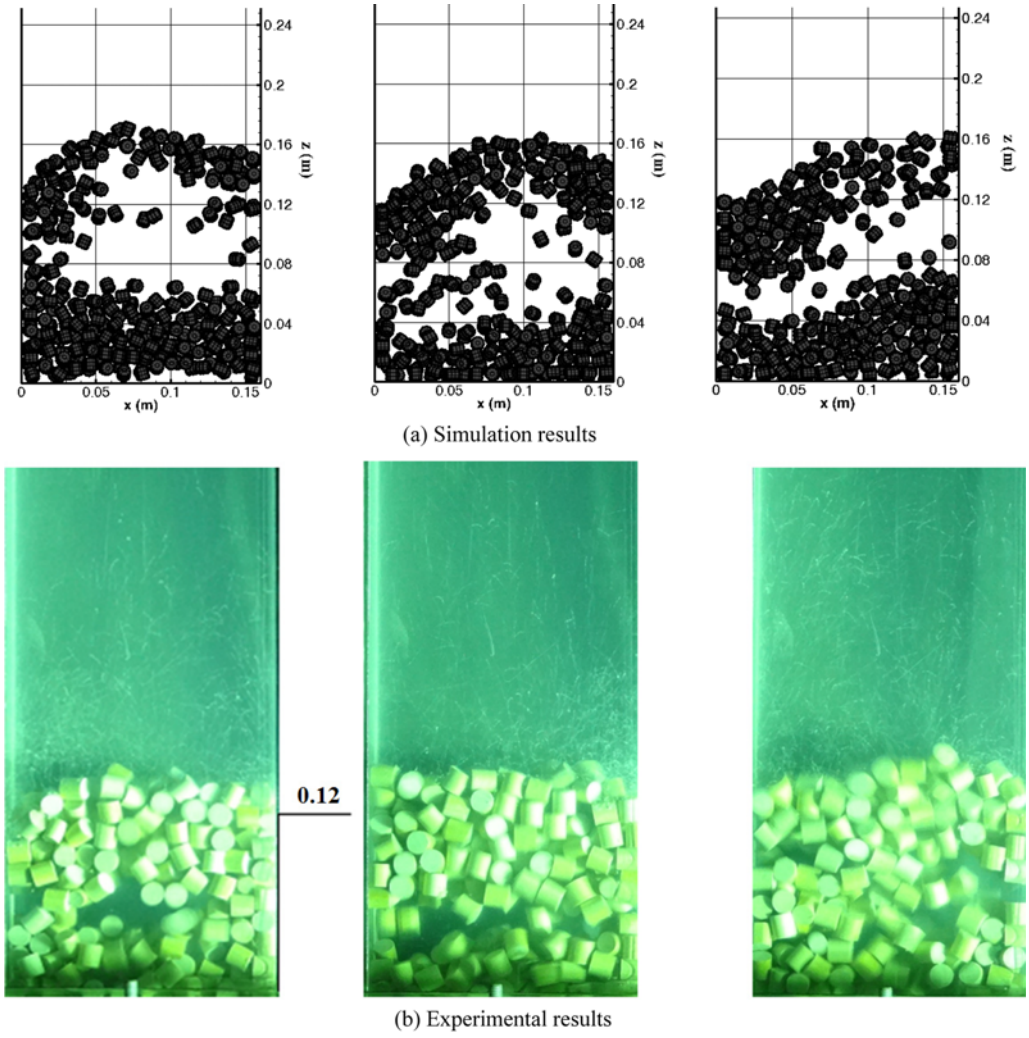

Fig. 10. Comparison of flow patterns in simulation results and experimental results (H_0=70 mm, u_s=2.8 m/s).

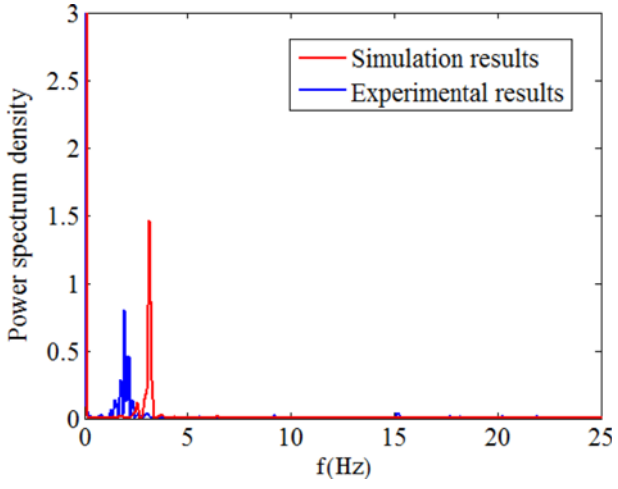

Fig. 11. Power spectrum density analysis of pressure fluctuation signals (H_0=70 mm, u_s=2.8 m/s).

[22]. This dominant frequency corresponds to the frequency of bubble motion.

Compared with the experimental results, the bed expansion height in the simulation results is higher. It illustrates that the gas-solid force in the simulation results is larger than that in a real situation. This simulation error can be reduced by increasing d_p/Δ [23], but because of the limitation of computation time, simulation work with smaller grid size was not performed.

2. Gas Flow Field Distribution

Fig. 12 shows the gas velocity distribution on the two-dimensional cross section of fluidized bed (different background colors in the figure correspond to different values of solid volume fraction, so some contacting areas between cylinder-shaped particles are not clearly identified). In the simulation results, the gas flow around the cylinder-shaped particle can be observed clearly, and the formation and development of vortices behind the particle is affected obviously by the neighboring particles. Although the grid size is only 1/15 cm in the simulation, it cannot meet the requirement of turbulent solution. So, we only analyzed the gas velocity distribution quantitatively.

Fig. 13 shows the gas vertical velocity distribution in the simulation results. Near the wall surface, because of the non-slip boundary condition, the gas velocity is very small. As the radial distance

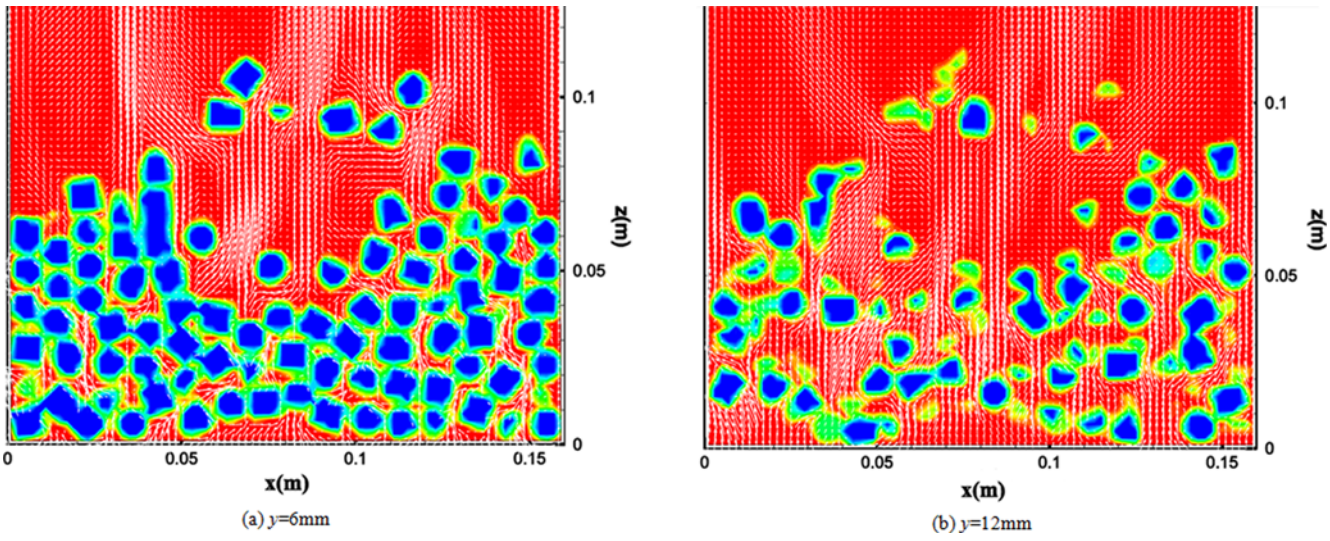

Fig. 12. Gas flow around the cylinder-shaped particles in fluidized bed.

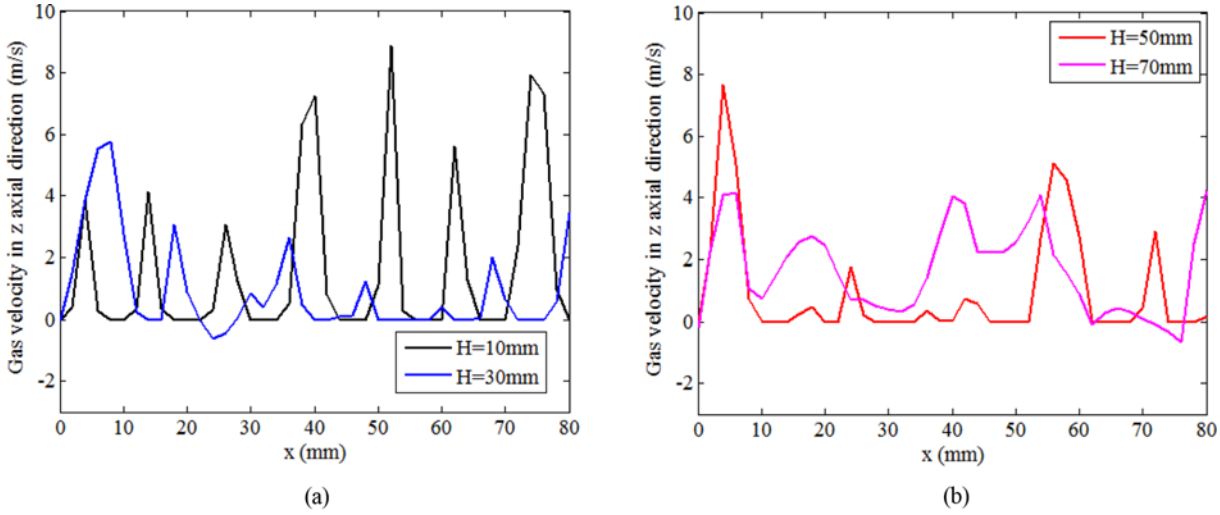

Fig. 13. Gas vertical velocity distribution in IBM-DEM simulation results (H_0=50 mm, u_s=2.8 m/s). (a) Low bed height; (b) high bed height.

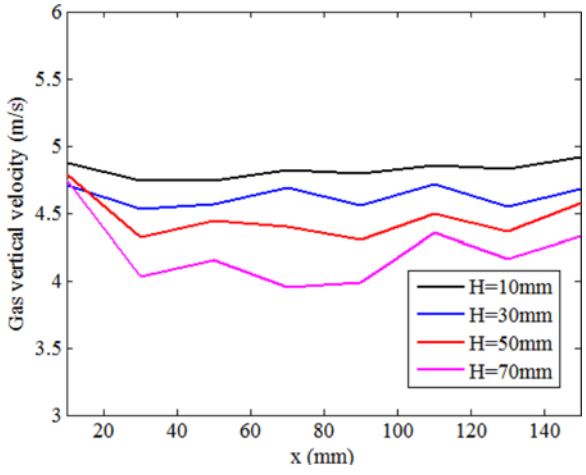

Fig. 14. Gas vertical velocity distribution in mesoscopic simulation results (H_0=50 mm, u_s=2.8 m/s).

increases, the gas velocity fluctuates. Inside the particle region, the void fraction and the gas velocity are both zero. Fig. 14 shows the gas vertical velocity distribution in mesoscopic CFD-DEM simulation results (for the accuracy of point-to-source model, the grid size for gas flow should be at least 2.0-2.5 times of particle size. The particle size is 10 mm, so, the grid sizes are selected as 20 mm). In mesoscopic CFD-DEM, the void fraction in each computation cell is less than 1.0 but much larger than 0.0, and the gas velocity in the cell is always larger than zero. Compared with IBM-DEM simulation results, the velocity profile is much smoother, but the non-slip boundary condition cannot be satisfied well. In fact, this grid size in current CFD-DEM is too coarse to solve the gas phase. Mesoscopic CFD-DEM is not suitable for the flow simulation of large particles.

3. Particle Translation Velocity

Fig 15(a) shows the particle vertical velocity distribution in the fluidized bed. In the central region (50 mm≤x≤100 mm), because

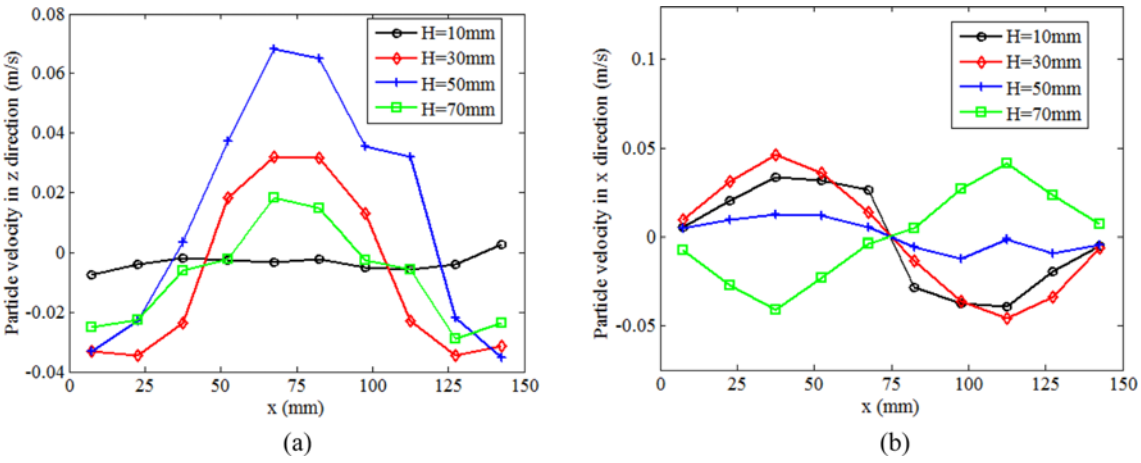

Fig. 15. Particle velocity distribution in the simulation results (H_0=50 mm, u_s=2.8 m/s). (a) Particle vertical velocity; (b) particle radial velocity.

of the effect of drag force, particles move upwards. As the height from the vessel bottom H is lower than 50 mm, the particle velocity increases with the increase of H. As H reaches about 50 mm, the gravity starts to exceed the drag force, and the particle velocity decreases with the increase of H. In the boundary region (x<50 mm or x>100 mm), because of the effect of particle gravity, particles move downwards. As H is higher than about 30 mm, particles fall with the accelerating velocity. However, for collision resistance, the falling velocity starts to reduce as H decreases to 30 mm. In all, the profile of the vertical velocity is very flat in the bottom region, but looks parabolic in the upper region.

Fig 15(b) shows the particle radial velocity distribution in the fluidized bed. In the central region (x=75 mm), the particle radial velocity is about zero. As the radial distance from the vertical axis increases, the particle velocity increases, and reaches a maximum value at x=40(120) mm. Once particles enter the wall region, be-

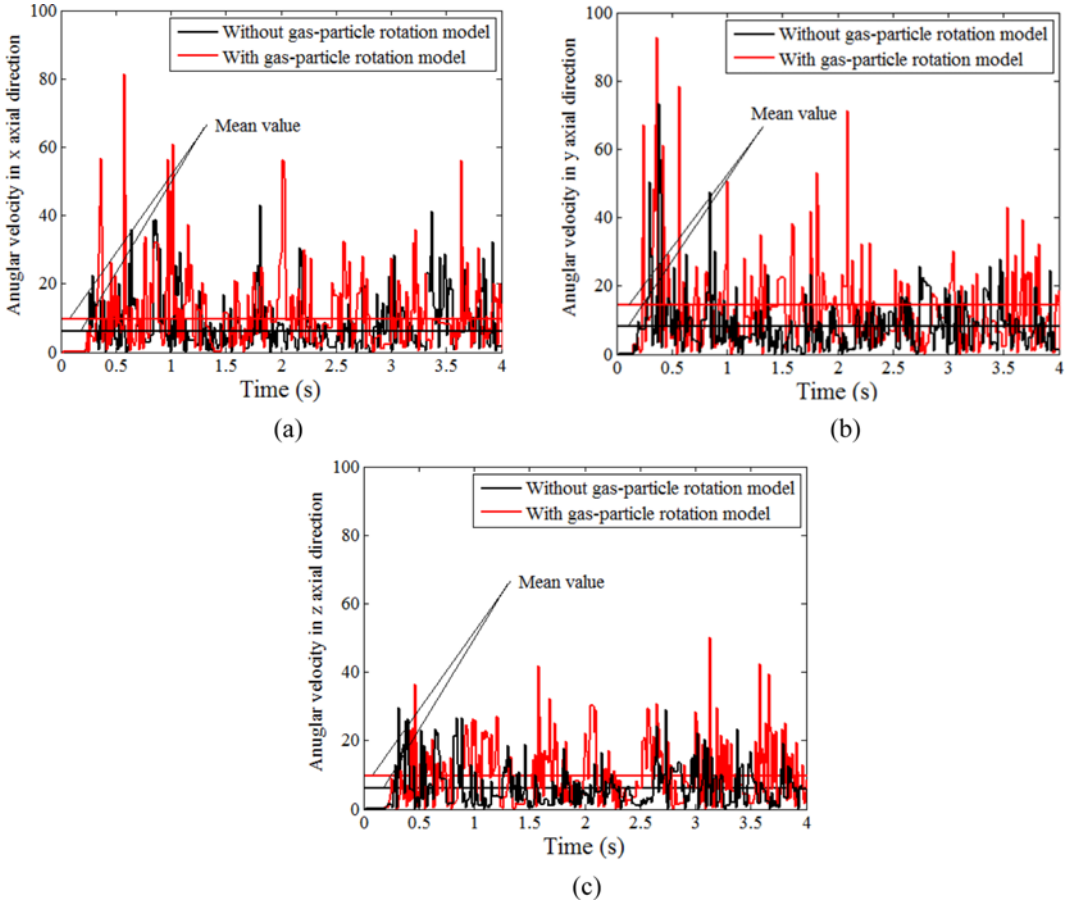

Fig. 16. Evolution of particle angular velocity in the simulation results. (a) x axial direction; (b) y axial direction; (c) z axial direction.

cause of the wall resistance, the velocity starts to reduce. At low height, particles move from the boundary region to the central region, but at high height, the moving direction is opposite.

4. Particle Angular Velocity

In mesoscopic simulation method, the particle is regarded as one point, and the gas-solid drag force cannot make the particle rotate, which is different from the actual condition. To investigate the gas effect on the particle rotation, we compared the particle angular velocity (absolute value) with and without the gas-particle rotation model in Fig. 16. The averaged angular velocity, $\mathbf{w}_{p,avg}$, was defined as:

$$\mathbf{w}_{p,avg}=\frac{\sum_{i=1}^{N}\mathbf{w}_{p,i}}{N} \tag{17}$$

where, $\mathbf{w}_{p,i}$ denotes the angular velocity of the ith particle, and N denotes the particle number. It can be found that the averaged value of the angular velocity with gas-particle rotation model is much larger than that without gas-particle rotation model. This means that the gas-solid interacting force plays an important role in particle rotation motion. In some previous researches, the effect of gas on the particle rotation is neglected. For small particles, the pressure gradient along the particle surface is not large, and this assumption is reasonable. However, for large particles, the gas-particle interacting force on the particle surface is not uniform, and this assumption is not suitable. It also can be found that the angular velocity in y axial direction is the largest: The vessel width is much larger than the depth, and the particle rotation along radial and vertical direction meets larger resistance.

5. Particle Trajectory

To investigate the particle trajectory, three particles in fluidized bed were tracked in the simulation results, and their initial positions are (65, 10, 5) mm, (5, 10, 5) mm and (65, 10, 25) mm. Fig. 17 shows the change of the particle position in vertical and radial direction with time, respectively. In vertical direction, the fluctuation of particle position is regular, and the fluctuation frequencies of the three different waves in Fig. 17(a) are very close. This frequency corresponds to the dominant frequency in spectrum analysis, and reflects the formation, growth and break-up of bubbles in a fluidized bed. In Fig. 17(b), particles a and b move from the central region to the boundary region, while the movement direction of particle c is opposite. There is momentum exchange between the boundary region and central region. The fluctuation of particle position in radial direction looks much more random compared with that in vertical direction, and no dominant frequency can be observed. Because the vessel is a quasi-three dimensional fluidized bed, the particle movement in y axial direction is not discussed.

CONCLUSIONS

IBM and DEM were coupled to simulate the flow of cylinder-shaped particle in fluidized bed. The gas-solid interacting force was calculated by solid volume-weighted method developed by Kajishima et al.

The gas velocity, particle velocity and particle trajectory in fluidized bed were analyzed in detail. Large cylinder-shaped particles are very difficult to fluidize, and slugging flow regime can be observed even if the static bed height is low. The velocity field of gas phase in a fluidized bed is analyzed on microscale, and the formation and development of vortex behind the particle is affected obviously by the neighboring particles. In previous point-to-source model, the effect of gas on the particle rotation was neglected. But in this research, we fouind that the gas effect on the rotation of large particles becomes active as particle size increases.

Compared with the experimental results, the gas-solid force in simulation results is larger. This is because the accuracy of solid volume-weighted method depends on the grid size, and the grid size in this research is only 1/15th of particle size. However, because of the limitation of calculation time, the simulation work with smaller grid size was not carried out.

ACKNOWLEDGEMENTS

The authors would like to thank the Fundamental Research Funds for the Central Universities (NS2015019) and the National Natural Science Fund Program of China (51276040) for financial support.

Some ideas were inspired during the authors' visit to Tanaka & Tsuji lab in Osaka University. The authors express their sincere thanks

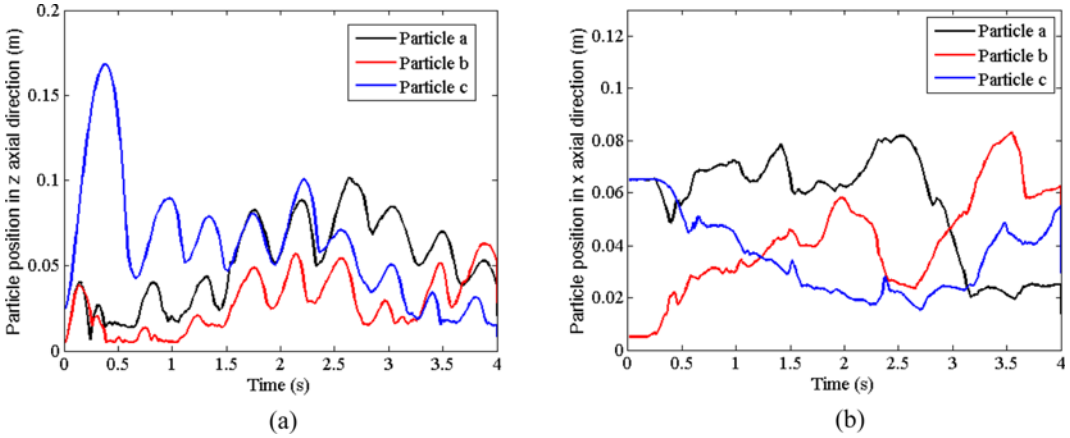

Fig. 17. Particle trajectory in the simulation results. (a) z axial direction; (b) x axial direction.

to Professors Toshitsugu Tanaka and Takuya Tsuji.

REFERENCES

1. Y. Tsuji, T. Kawaguchi and T. Tanaka, *Powder Technol.*, **77**, 79 (1993).
2. P. A. Cundall and O. D. L. Strack, *Geotechnique*, **29**, 47 (1979).
3. H. P. Zhu, Z. Y. Zhou, R. Y. Yang and A. B. Yu, *Chem. Eng. Sci.*, **63**, 5728 (2008).
4. H. S. Zhou, G. Flamant and D. Gauthier, *Chem. Eng. Sci.*, **59**, 4193 (2004).
5. S. L. Yang, K. Luo, M. M. Fang, K. Zhang and J. R. Fan, *Chem. Eng. J.*, **236**, 158 (2014).
6. C. H. Wang, Z. P. Zhong and X. Y. Wang, *Can. J. Chem. Eng.*, **92**, 1488 (2014).
7. H. Nakamura and S. Watano, *Powder Technol.*, **171**, 106 (2007).
8. K. Kuwagi, H. Utsunomiya, Y. Shimoyam, H. Hirano and T. Takami, *The 13th international conference on fluidization-new paradigm in fluidization engineering* (2010).
9. M. A. van der Hoef, M. van Sint Annaland, N. G. Deen and J. A. M. Kuipers, *Annu. Rev. Fluid Mech.*, **40**, 47 (2008).
10. J. S. Ma, W. Ge, Q. G. Xiong, J. W. Wang and J. H. Li, *Chem. Eng. Sci.*, **64**, 43 (2009).
11. L. M. Wang, G. F. Zhou, X. W. Wang, Q. G. Xiong and W. Ge, *Particuology*, **8**, 379 (2010).
12. C. S. Peskin, *J. Comput. Phys.*, **25**, 220 (1977).
13. Z. L. Wang, J. R. Fan and K. Luo, *Int. J. Multiphase Flow*, **34**, 283 (2008).
14. T. Kempe and J. Frohlich, *J. Comput. Phys.*, **231**, 3663 (2012).
15. B. E. Griffith, X. Y. Luo, D. M. McQuee and C. S. Peskin, *Int. J. Appl. Mech.*, **1**, 137 (2009).
16. Y. Guo, C. Y. Wu and C. Thornoto, *AIChE J.*, **59**, 1075 (2013).
17. T. Kajishima, S. Takiguchi, H. Hamasaki and Y. Miyaka, *JSME Int. J.*, **44**, 526 (2001).
18. Y. Tsuji, T. Tanaka and T. Ishida, *Powder Technol.*, **71**, 239 (1992).
19. A. Dziugys and B. Peters, *Granular Matter.*, **3**, 231 (2001).
20. H. Tao, W. Q. Zhong and B. S. Jin, *Proceedings of CSEE*, **32**, 13 (2012).
21. R. D. Mindlin, *J. Appl. Mech.*, **16**, 259 (1949).
22. A. I. Karamavruc and N. N. Clark, *Chem. Eng. Sci.*, **52**, 357 (1997).
23. T. Tsuji, H. Yada, K. Yoshikawa and T. Tanaka, *7th International Conference on Multiphase Flow* (2010).